

A differential structure approach to membrane segmentation in electron tomography

Antonio Martinez-Sanchez^a, Inmaculada Garcia^b, Jose-Jesus Fernandez^{c,*}

- ^a*Supercomputing and algorithms group. Associated Unit CSIC-UAL, University of Almeria,
04120 Almeria, Spain*
- ^b*Supercomputing and algorithms group. Dept. Computer architecture. University of Malaga,
29080 Malaga, Spain*
- ^c*National Centre for Biotechnology. National Research Council (CNB-CSIC). Campus UAM.
Darwin 3. Cantoblanco. 28049 Madrid. Spain.*
-
-

*Corresponding author:
National Centre for Biotechnology.
National Research Council (CNB-CSIC).
Campus UAM. Darwin 3. Cantoblanco.
28049 Madrid. Spain.
Tel: +34 91 585 4619. Fax: +34 91 585 4506
Email: jj.fernandez@csic.es

Abstract

Electron tomography allows three-dimensional visualization of cellular landscapes in molecular detail. Segmentation is a paramount stage for the interpretation of the reconstructed tomograms. Although several computational approaches have been proposed, none has prevailed as a generic method and thus segmentation through manual annotation is still a common choice. In this work we introduce a segmentation method targeted at membranes, which define the natural limits of compartments within biological specimens. Our method is based on local differential structure and on a Gaussian-like membrane model. First, it isolates information through scale-space and finds potential membrane-like points at a local scale. Then, the structural information is integrated at a global scale to yield the definite segmentation. We show and validate the performance of the algorithm on a number of tomograms under different experimental conditions.

Key words

Segmentation , Image Processing , Electron Tomography , Membrane , Scale-Space

1. Introduction

Electron tomography (ET) has consolidated its position as the leading technique for visualizing the molecular organization of the cell environment (Lucic et al., 2005; Frank, 2006; Barcena and Koster, 2009; Ben-Harush et al., 2010). The computational stages to derive three-dimensional reconstructions (or tomograms) from the acquired images are well established (Lucic et al., 2005). Nevertheless, their interpretation is not straightforward due to different factors such as the limited tilt range conditions, the low signal-to-noise ratio (SNR, which is particularly poor in cryoET) and the inherent biological complexity. Significant efforts are thus spent to facilitate the interpretation by several stages of post-processing of the tomograms (Volkman, 2010), which, in the particular case of pleomorphic structures, are primarily noise reduction and segmentation.

Noise reduction intends to improve the SNR and, though there are several alternative methods (e.g. van der Heide et al., 2007; Fernandez, 2009), anisotropic nonlinear diffusion has become the standard tool in the field (Frangakis and Hegerl, 2001; Fernandez and Li, 2003, 2005). The SNR of the tomogram and the denoising method have an influence on the performance of the subsequent segmentation process (Volkman, 2010). In addition, segmentation is also affected by the artefacts due to the limited tilt range in ET (the ‘missing wedge’ in Fourier space), which produce a significant loss of resolution of the tomogram along the beam direction, thereby making the spatial features in that direction look elongated and blurred.

Segmentation aims to decompose the tomogram into its structural components by identifying the sets of voxels that constitute them. Though tedious and subjective, manual segmentation is the simplest and the most common approach,

which consists in that the user assigns the structural features using visualization tools (e.g. [He et al., 2008](#)). Several automatic or semi-automatic approaches have been proposed in the field ([Sandberg, 2007](#); [Volkman, 2010](#)). There exist methods based on simple density thresholds ([Sandberg, 2007](#)) or more sophisticated optimal thresholding ([Cyrklaff et al., 2005](#)), the Watershed transform extended to 3D ([Volkman, 2002](#)), eigenvector analysis of an affinity matrix ([Frangakis and Hegerl, 2002](#)), active contours ([Bartesaghi et al., 2005](#)), oriented filters ([Sandberg and Brega, 2007](#)) and fuzzy logic ([Garduno et al., 2008](#)). Also, template matching with simple 3D geometric templates has been proposed for tomograms with relatively good SNR and contrast ([Lebbink et al., 2007](#)). Recent reviews discuss about the characteristics, advantages and drawbacks of the different segmentation techniques presented so far in the field ([Sandberg, 2007](#); [Volkman, 2010](#)). Out of all computational methods, the Watershed transform is perhaps the only one that has achieved a fairly good level of dissemination ([Volkman, 2010](#)) and even has been used as a basis to develop further methods or tools ([Salvi et al., 2008](#); [Fernandez-Busnadiego et al., 2010](#)). Despite the wealth of methods available and their potential, none has stood out as a general applicable method yet, and manual segmentation still remains the prevalent method. Most popular ET software packages incorporate intuitive graphical tools to assist the user to segment and annotate tomograms, and progressively they are incorporating some of the most known computational techniques (namely, thresholding and the Watershed transform) in order to make segmentation a semi-automatic process.

Detection of membranes plays an important role in segmentation as they encompass compartments within biological specimens, define the limits of the intracellular organelles and the cells themselves, etc.. Several segmentation ap-

proaches presented in the field are well suited to membrane detection. The oriented filters ([Sandberg and Brega, 2007](#)) showed promising results, but it worked in 2D on a slice-by-slice basis and the 3D models were then created by stacking the membrane contours. Template matching with cuboid-shaped templates ([Lebink et al., 2007](#)) managed to segment fairly well membranes with high contrast. However, this is not the case in cryoET. Furthermore, it was computationally intensive and high performance computing ([Fernandez, 2008](#)) was necessary. These two methods have not proved to be robust to deal with high membrane curvature either. The Watershed transform has shown good performance in segmenting membranous structures, such as the Golgi apparatus in good contrast tomograms ([Volkman, 2002](#)). Nevertheless, such performance has not been exhibited under high noise, low contrast conditions, as reported recently ([Moussavi et al., 2010](#)). The latter work combined template matching with an elliptical model for the cell membrane and succeeded in extracting the cell boundaries. Nevertheless, it is so specific that it could not be applied for a general case involving any type of membrane-bound organelle. Some other work combined the Watershed transform with an energy-based approach ([Nguyen and Ji, 2008](#)), but user intervention was still required and there were a number of parameters difficult to tune.

In this work we present an algorithm for membrane segmentation that relies on local differential structure. The method produces an output map that represents how well every point in the tomogram fit a membrane model. From this map, the definite segmentation is obtained. We evaluate the performance of the algorithm on a number of tomograms under different SNR and contrast conditions.

2. Membrane model

At a local level, a membrane can be considered as a plane-like structure with certain thickness (Fernandez and Li, 2003, 2005). The density along the normal direction progressively decreases as a function of the distance to the centre of the membrane. This density variation across the membrane can be modelled by a Gaussian function (Fig. 1(a,b)) and can be expressed as:

$$I(r) = \frac{D_0}{\sqrt{2\pi}\sigma_0} e^{-\frac{r^2}{2\sigma_0^2}} \quad (1)$$

where r runs along the direction normal to the membrane, D_0 is a constant to set the maximum density value (at the centre of the membrane) and σ_0 is related to the membrane thickness.

The eigen-analysis of the structure tensor of the density function at the point $p = (x, y, z)$ of the membrane yields the eigenvectors \vec{v}_1 , \vec{v}_2 and \vec{v}_3 with eigenvalues $|\mu_1| \gg |\mu_2| \approx |\mu_3|$ (Fig. 1(a)) (Fernandez and Li, 2003, 2005). This reflects that there are two directions (\vec{v}_2 , \vec{v}_3) with small density variation and the largest variation runs along the direction perpendicular to the membrane (\vec{v}_1 , parallel to r , i.e. $\vec{v}_1 \parallel r$).

The membrane thickness is modelled by means of σ_0 . It is important for a detector based on this membrane model to have this parameter properly tuned so as to increase its robustness and selectivity. It is usually set up as the typical thickness of a membrane (in pixels) within the tomogram.

Due to its local nature, any detector based on this model can also generate a high response for structures different from membranes. This is particularly true in ET where these other structures (e.g. microtubules, actin filaments, etc.) also tend to look like planes at a local level due to the artefacts produced by the missing

wedge, as already shown and accounted for (Fernandez and Li, 2003). For that reason, it is important to incorporate “global information” in order to discern true membranes from these other structures.

3. Algorithm for membrane detection

The algorithm comprises a number of stages that can be grouped into two main blocks. Fig. 2 shows a flow diagram of the algorithm. The first three stages are intended to isolate information at a suitable scale and find potential membrane-like features according to local detectors. The two last stages are, however, aimed to analyze and integrate the structural information at a global scale. In the following, the different stages are described in detail. **The procedure assumes that high grey-scale levels represent electron dense objects.**

3.1. Scale-space

The scale-space theory was formulated in the 80s (Witkin, 1983; Koenderink, 1984) and allows isolation of the information according to the spatial scale. At a given scale σ , all the features with a size smaller than the scale are filtered out whereas the others are preserved (Fig. 3).

For discrete signals, a scale-space can be generated by the method proposed by Lindeberg (1990). Mathematically speaking, a tomogram can be modelled as a discrete function $f : C \subseteq \mathbb{Z}^3 \rightarrow \mathbb{R}$, so a scale-space of f would be a continuous set of tomograms $L : C \subseteq \mathbb{Z}^3 \times \mathbb{R}^+ \rightarrow \mathbb{R}$ that can be obtained by convolution of f and a set of kernels, $T : \mathbb{Z}^3 \times \mathbb{R}^+ \rightarrow \mathbb{R}$, with size $\sigma > 0$:

$$L(x, y, z, \sigma) = \sum_{n=-\infty}^{\infty} \sum_{m=-\infty}^{\infty} \sum_{q=-\infty}^{\infty} T(n, m, q; \sigma) f(x - n, y - m, z - q) \quad (2)$$

with $L(x, y, z; 0) = f(x, y, z)$.

There are a number of requirements for a function to act as a kernel in constructing a scale-space (Lindeberg, 1990) (e.g. symmetry, semi-group, normalization, stability). In this work, the implementation of the scale-space relies on a direct convolution with a sampled Gaussian kernel. In addition, this convolution has been implemented by means of recursive filters (Young and van Vliet, 1995) and exploiting the separability property of the Gaussian kernel, which allows reduction of the computational complexity.

The scale-space applied to the membrane model proposed in the previous section is now analyzed. Assume without loss of generality that r runs along the x direction (i.e. $\vec{v}_1 \parallel r \parallel x$), that $\lambda_2 \approx \lambda_3 \approx 0$ and that $|\lambda_1| > 0$. These assumptions allows reduction of the problem to the one-dimensional case. Given the continuous signal $I : \mathbb{R} \rightarrow \mathbb{R}$ (coming from the membrane model with thickness σ_0), its scale-space $L : \mathbb{R} \times \mathbb{R}^+ \rightarrow \mathbb{R}$ at the scale $\sigma > 0$ is defined by (Koenderink, 1984):

$$L(x; \sigma) = G(x; \sigma) * I(x) \quad (3)$$

with

$$G(x; \sigma) = \frac{1}{\sqrt{2\pi}\sigma} e^{-\frac{x^2}{2\sigma^2}} \quad (4)$$

Note that $I(r)$ can be replaced by $I(x)$ since $r \parallel x$ is assumed. The convolution of two continuous Gaussian functions like I and G yields another Gaussian function whose variance is the sum of the variances of the two convolved functions (Florack et al., 1992), hence verifying the semi-group scale-space property. Therefore, and ignoring **multiplicative** constants, the membrane model with thickness σ_0 at a scale σ can be expressed as:

$$L(x; \sigma) = G(x; \sqrt{\sigma^2 + \sigma_0^2}) \quad (5)$$

In this work, we assume that all the targeted membranous features have a similar size. Therefore, just one scale σ is enough. This parameter is usually set up as $\sigma = \sigma_0$ in order to filter out features with a size smaller than the membranes being sought. If features with very different size were to be detected, several rounds of the algorithm using the appropriate scales should be run. Each run would be in charge of detecting features at the given scale.

3.2. Local detector

Once we know what the membrane model at a given scale σ looks like (Eq. (5)), it is possible to define a detector for it. This detector is based on differential information, as it has to analyze local structure. In order to make it invariant to the membrane direction and curvature, the detector is established along the direction normal to the membrane (i.e. the direction of the maximum curvature) at the local scale. An eigen-analysis of the Hessian matrix is well suited to determine such direction (Sato et al., 1998; Frangi et al., 1998). At every single voxel of the tomogram, the Hessian matrix is calculated as defined by:

$$H = \begin{bmatrix} L_{xx} & L_{xy} & L_{xz} \\ L_{xy} & L_{yy} & L_{yz} \\ L_{xz} & L_{yz} & L_{zz} \end{bmatrix} \quad (6)$$

where $L_{ij} = \frac{\partial^2 I}{\partial i \partial j} \forall i, j \in (x, y, z)$. The Hessian matrix provides information about the second order local intensity variation. The first eigenvector v_1 resulting from the eigen-analysis is the one whose eigenvalue λ_1 exhibits the largest absolute value and points to the direction of the maximum curvature (second derivative). Detection of zero-crossings in the second derivative along that direction allows estimation of the limits of the potential membrane (Fig. 1(c)).

The Hessian matrix of the membrane model of the previous section (i.e. with direction of the maximum curvature along x) at a scale σ has all directional derivatives null, except L_{xx} :

$$H = \begin{bmatrix} L_{xx} & 0 & 0 \\ 0 & 0 & 0 \\ 0 & 0 & 0 \end{bmatrix} \quad (7)$$

with

$$L_{xx} = \frac{D \left(x^2 - (\sigma^2 + \sigma_0^2) \right)}{\sqrt{2\pi}(\sigma^2 + \sigma_0^2)^{5/2}} e^{-\frac{x^2}{2(\sigma^2 + \sigma_0^2)}} \quad (8)$$

where D denotes the constants ignored in Eq. (5). As a result, $\lambda_1 = L_{xx}$ and $\vec{v}_1 = (1, 0, 0)$. Along the direction normal to the membrane, λ_1 turns out to be negative where the membrane has significant values and its absolute value progressively decreases from the centre towards the extremes of the membrane, as shown in Fig. 1(c).

This derivation leads us to propose the use of $|\lambda_1|$ as a local membrane detector (also known as local gauge). In practice, in experimental studies λ_2 and λ_3 are not null, though $|\lambda_1| \gg |\lambda_2| \approx |\lambda_3|$ holds. Therefore, a more realistic gauge would be:

$$R = \begin{cases} |\lambda_1| - \sqrt{\lambda_2 \lambda_3} & \lambda_1 < 0 \\ 0 & \lambda_1 \geq 0 \end{cases} \quad (9)$$

where $\sqrt{\lambda_2 \lambda_3}$ is the geometrical mean between λ_2 and λ_3 .

3.3. Membrane strength

Unfortunately, the gauge R is still sensitive to other local structures that may produce false positives along the maximum curvature direction. To make the gauge robust and more selective, it is necessary to define detectors for these cases.

First, the noisy background in the tomogram may generate false positives. However, the background usually has a density level different from that shown by the structures of interest, which is especially apparent at higher scales (Fig. 3). A strategy based on density thresholding, as already used for denoising (Fernandez and Li, 2005), helps to get rid of these false positives. This threshold t_l is applied over the scale-space representation of the tomogram L instead of the original tomogram itself f for further robustness to noise.

Local structures resembling ‘density steps’ in the tomogram also make the gauge R produce a false peak (see Appendix A). A detector of a local step could be the edge saliency, which reflects the gradient strength (Lindeberg, 1998):

$$S = L_x^2 + L_y^2 + L_z^2 \quad (10)$$

where $L_i = \frac{\partial L}{\partial i} \forall i \in (x, y, z)$. A membrane exhibits a high value of S at the extremes and a low value at the centre (Fig. 1(d)). Based on their response to a membrane, the ratio between the squared second-order and first-order derivatives (i.e. R^2/S) quantifies how well the local structure around a voxel fits the membrane model and not a step. We thus define membrane strength as:

$$M = \begin{cases} \frac{R^2}{S} & , (L > t_l) \text{ and } \left(\text{sign} \left(\frac{\partial R}{\partial r} \right) \neq \text{sign} \left(\frac{\partial S}{\partial r} \right) \right) \\ 0 & , \text{otherwise} \end{cases} \quad (11)$$

The first condition in Eq. (11) denotes the density thresholding described above. The second condition represents the requirement that the slopes of R and S in the gradient direction must have opposite signs. **This condition is important to restrict the response of that function for steps (see Appendix A), which will be definitely removed in the subsequent stage.** If the local structure approaches the membrane model, M will have high values around the centre of the membrane

(high values of R^2 , low values of S). Note that the ratio R^2/S strictly embodies differential information and thus does not depend on the actual density values. The information about the density is then introduced into M by means of the condition $L > t_l$. In practice, the ratio is actually implemented as $R^2/(S + \epsilon)$ to prevent division by 0, where $\epsilon > 0$ is sufficiently small.

3.4. Improved hysteresis thresholding

The next step intends to threshold the membrane strength so that voxels with low values of M are definitely discarded. Hysteresis thresholding has been shown to outperform the standard thresholding algorithm (Sandberg, 2007). Here two thresholds are used, the large value t_u undersegments the tomogram whereas the other t_o oversegments it. Starting from the undersegmented tomogram (seed voxels), adjacent voxels are added to the segmented tomogram by progressively decreasing the threshold until the oversegmenting level t_o is reached. **Though this procedure performs better than the standard thresholding algorithm, the undersegmented tomogram still contains spurious segments that may spoil the final segmentation result.**

In this work we have increased the robustness of hysteresis thresholding by constraining the selection of seed voxels to the particular characteristics of membranes, as described in the following. Membranes comprise a high number of voxels connected in 3D. When the tomogram is viewed plane-by-plane along any axis, the voxels of the membranes also appear connected in those individual 2D planes. **Therefore, a threshold t_{N2} over the number of voxels that appear connected in 2D planes helps to remove isolated points or marginal segments that may arise as a result of the conventional undersegmentation process.** Only sets with a number of connected voxels higher than t_{N2} are thus preserved. This area-

thresholding process is applied planewise along all the axes (X, Y and Z). Next, the definite set of seeds is obtained through another similar thresholding procedure, this time with a threshold t_{N3} over the volume, to discard 3D components with less than t_{N3} connected voxels. The conventional hysteresis thresholding process then proceeds (see Appendix B). This strategy allows isolation of seeds that are most representative of membranes (Fig. 4), thereby improving the robustness of the whole algorithm.

3.5. Global analysis

The result of the previous step is a logical map (i.e. true/false) indicating the voxels of the tomogram that have been identified as membranes or, more precisely planes, at a local scale. This step then aims to identify the segmented components (sets of connected voxels labelled as true) and carry out a global analysis in order to discern whether they are actual membranes.

A distinctive attribute shared by membranes is their relatively large dimensions. Therefore, the size (i.e. the number of voxels of the component) can serve as a major global descriptor for membranes. A threshold t_v is then introduced to set the minimal number of voxels for a segmented component to be considered as membrane. This threshold is related to t_{N3} in the previous step. If the tomogram only contains one membrane, these two thresholds may be similar or equal. If the tomogram contains several membranes, different values of t_v allow their segmentation separately.

4. Validation

Validation of segmentation algorithms is a difficult topic, as already discussed in the field (Sandberg, 2007; Sandberg and Brega, 2007; Garduno et al., 2008).

Most of the segmentation works demonstrate the performance of the methods according to illustrative visual results. [Garduno et al. \(2008\)](#) first addressed the topic and proposed objective criteria to compare the automatic method versus the “ground truth” given by manual segmentation. Other works have proposed and adapted metrics based on similar ideas ([Nguyen and Ji, 2008](#); [Moussavi et al., 2010](#)).

The criteria defined by [Garduno et al. \(2008\)](#) are strongly based on the overlap between the segmented data and the ground truth. This is problematic for relatively thin structures, such as membranes, where differences of just one single voxel in distance may spoil these criteria (e.g. the overlap between two hollow spheres with one-voxel-thick walls, placed at the same centre and with a difference in radius of just 1 voxel is null). This may be especially delicate when freehand manual segmentation (where the delineation may not be precise) is employed as ground truth, as done in the present work.

For that reason, here we validate our segmentation method focusing on the outlined shapes. Quality metrics are defined based on the following features typically applied in shape analysis ([Teague, 1980](#)):

- Centroid: centre of mass.
- Bounding box: centre, width and height of the **smaller rectangular box containing the shape**.
- Axes (major and minor): length of the axes of the ellipse with the same normalized second central moment as the shape.

The metrics reflecting the agreement between the features delineated by our

method versus the ground truth are defined based on the relative error, as follows:

$$100 \cdot \left(1 - \frac{1}{\sum_{p=1}^{N_p} w_a(p)} \sum_{p=1}^{N_p} w_a(p) \frac{\|v_{f,g}(p) - v_{f,a}(p)\|}{v_{f,g}(p)} \right) \quad (12)$$

where f denotes one of the features described above, $v_{f,g}$ is the estimated value for property f in the ground truth, and $v_{f,a}$ is the value for the result obtained by our algorithm. The metrics are calculated planewise along the X, Y and Z axes, as reflected by the index p in that equation. A weighted average is finally computed over the whole set of N_p planes using the area of the ground truth shapes, denoted by $w_a(p)$, as a weight.

Another feature commonly found in shape analysis is the convex hull, which is the smallest convex polygon that contains the shape. The use of the hull allows the application of the criteria defined by [Garduno et al. \(2008\)](#) and [Udupa et al. \(2006\)](#) ameliorating the problematic situation described above. We can then estimate the sensitivity, i.e. the fraction of true positives (TPF, points that have been correctly classified as inside of the object) and the specificity, i.e. the fraction of true negatives (TNF, points that have been correctly left out of the object). Let H_g and H_a be [the convex hull](#) of the ground truth and the segmentation resulting from our algorithm, respectively. These metrics are defined using algebra of sets as, respectively:

$$\text{TPF} = \frac{|H_a \cap H_g|}{|H_g|} \quad (13)$$

$$\text{TNF} = \frac{|H_a^C \cap H_g^C|}{|H_g^C|} \quad (14)$$

where $|\cdot|$ denotes cardinality, \cap represents the set intersection operation, and A^C denotes the complement of set A . [Note that TNF is influenced by the size of](#)

the tomogram (Udupa et al., 2006). In this work, TPF and TNF are calculated planewise along the X, Y and Z axes, and a weighted average is finally computed, as above (Eq. 12), to yield the actual values of sensitivity and specificity, respectively.

5. Results

The segmentation algorithm was tested with several tomograms taken under different experimental conditions, including cryo-tomography and the use of contrast agents. The tomograms were preprocessed to rescale the density to a common range of $[0, 1]$, with high values representing electron dense objects. They were also cropped to focus on an area of interest. No other preprocessing was applied to the tomograms (e.g. denoising). The optimal results were obtained using the same basic parameter configuration for hysteresis thresholding, in particular $t_u \in [0.25, 0.35]$, $t_o \in [0.05, 0.15]$ and $t_{N2} \in [15, 35]$. The values of the parameters σ , t_l , t_{N3} and t_v , however, depend on the specific dataset. Their values can be readily estimated by inspection of the tomogram under study. σ is the thickness of the membrane. t_{N3} and t_v are the minimal cardinality for a set of 3D-connected voxels to be considered as a membrane. Their values are similar unless more than one membrane are to be detected, in which case t_v is used to distinguish among them. t_l is a density threshold and can be estimated directly from an area of background in the tomogram and is typically in the range $[0.3, 0.5]$.

5.1. *Dictyostelium discoideum*

The first test dataset was a cryo-tomogram of *D. discoideum* cell (Medalia et al., 2002). It was obtained thanks to cryoET, where the SNR and contrast are particularly poor. Fig. 5 shows the result of the different stages of the algorithm

applied to the tomogram. A scale of $\sigma = 3$ was used for the scale-space (see Fig. 3). A lower scale cannot completely remove spurious structures. A higher scale would further smear out the actin filaments, still preserving the membranes.

Fig. 5(a) presents the gauge R , which actually quantifies the level of local membrane-ness. However, it is important to note that this measure does depend on the density level and, thus, there are some parts of the membrane where R exhibits weak values. On the contrary, M in Fig. 5(c) (or more precisely the ratio R^2/S) only contains differential information and, therefore, high strength is shown throughout the membrane regardless of the density value. However, the side effect is that other structures that do like planes at local level also produce a high value of M . The hysteresis thresholding procedure (Fig. 5(d-f)) and the global analysis manage to extract the true membranes (Fig. 5(g,h), yellow). The behaviour described in this paragraph can be readily observed in the other datasets too as this is an inherent feature of the algorithm.

The algorithm, as most of the segmentation methods, is sensitive to the effects of the missing wedge. As seen in Fig. 5(h), a region of the membrane appears broken because the density fades away due to its specific orientation (the normal to the membrane tends towards the beam direction). On the other hand, the missing wedge also makes the actin filaments look like planes at local scales. By using a different value for the threshold on the size of the components t_v , these actin filaments can also be extracted from the tomogram using the same segmentation approach (pink).

5.2. *Vaccinia virus*

The performance of the algorithm was also tested with a cryo-tomogram of *Vaccinia virus* (Cyrklaff et al., 2005). The algorithm succeeded in segmenting

both the outer and the core membrane by properly tuning the parameter σ , as seen in Fig. 6(c). As mentioned above, the results are affected by the missing wedge, as reflected by the fact that the membranes appear open along the beam direction.

A scale of $\sigma = 3$ was applied to extract the outer membrane. For the core membrane, however, a much higher value was necessary ($\sigma = 6$) because this membrane actually comprises two layers, the inner one is consistent with a lipid membrane whereas the outer is made up of a palisade of spikes anchored to the inner one (Cyrklaff et al., 2005). These two layers, together with some material at the inner facet, makes the boundary of the core rather thick (see Fig. 6(a,b)), thereby needing a higher scale to extract it separately. Fig. 6 also shows the intermediate results from some of the different stages of the algorithm (R , S , M). Results from the stages of the hysteresis thresholding are shown in Fig. 4.

5.3. *Human immunodeficiency virus*

The last cryo-tomogram contained HIV-1 virions (Briggs et al., 2006) and was taken from the EM databank (<http://emdatbank.org>; entry emd-1155). The tomogram required a scale of $\sigma = 2$ to segment the outer membranes. Fig. 7 presents the results of the algorithm, where the effect of the missing wedge is again apparent. In this particular dataset, segmentation of the membranes of the inner core was particularly challenging. This was caused by the fact that there was dense material in the interior and in close contact to the walls of the core, thereby precluding their extraction through the two latest steps of the algorithm.

5.4. *Golgi apparatus*

This dataset was taken from the Cell Centered DataBase (<http://ccdb.ucsd.edu>; entry 3632), which had an immunological synapse of cytotoxic T cell (Stinchcombe et al., 2006). To test the performance of the algorithm to segment mem-

branes, we focused solely on a Golgi apparatus. We had special interest in this structure because the manual segmentation is available at the CCDB site, which allows us to make a quantitative evaluation, as described below.

The algorithm was applied at a scale $\sigma = 2.2$ and was capable of segmenting the sought structure as only one component including all cisternae (Fig. 8). The algorithm actually detects the different membranes, or any planar structure in general, present in the tomogram such as those of the [surrounding mitochondria](#) (Fig. 8(c)). By means of the threshold t_v at the global analysis stage, the Golgi apparatus is isolated.

5.5. *Mitochondrion*

A tomogram of mitochondrion was also tested ([Perkins et al., 1997](#)). The algorithm, at a scale $\sigma = 1.7$, delineated the outer membrane as well as the inner cristae (pink), as shown in Fig. 9. In this particular case, it was not obvious to clearly separate the outer membrane (yellow) from the other membranous structures with t_v because the interaction between them is very tight. As shown in Fig. 9, their separation [causes](#) that the outer membrane has to appear broken.

5.6. *Mesoporous silica*

In order to show that the algorithm developed in this work is useful for electron tomography in general, not only in life sciences, we chose a dataset from Materials sciences. Electron tomography of ordered mesoporous silica helps to reveal its lattice structure and study the distribution of nanoparticle catalysts along the nanopores of the silica ([Midgley et al., 2007](#)). The study of the structure of such silica is essential for the understanding of complex catalyst systems and their characterization. Our algorithm is well suited to visualize the lattice structure of the silica in 3D directly from the raw tomogram as it easily segments the walls of the

nanopores (Fig. 10). A simple density threshold directly allows identification of the nanoparticles. In this tomogram, the algorithm worked at a scale of $\sigma = 2.2$.

5.7. Quantitative validation

To carry out a quantitative analysis of the performance of the algorithm, we selected the tomograms of Vaccinia virus and Golgi apparatus to make a comparison against the manual segmentation under different contrast conditions. In the former case, we did the delineation some time ago (Cyrklaff et al., 2005; Fernandez et al., 2006), and here we have only considered the outer membrane of the virion. In the latter, the contours were available at the CCDB (<http://ccdb.ucsd.edu>; entry 3632). We measured the metrics defined in Section 4, and obtained the results summarized in Table 1. The algorithm turns out to be similar to manual annotation in terms of shape analysis, with the quality indexes always higher than 90%. In particular, the centroid and the bounding box are defined precisely (around 97%). As far as the TPF and TNF metrics are concerned, the results obtained suggest that the method presented here is highly specific (TNF higher than 97%). In other words, the method successfully determines the regions that are not membranes. Furthermore, these results also confirm that the method is highly sensitive (TPF higher than 92%), which means it correctly delineates the membranes.

6. Discussion and conclusion

An algorithm to segment membranes in tomograms has been presented. It relies on a simple local membrane model and the local differential structure to determine points whose neighbourhood resembles plane-like features. **Those points are then further analyzed to determine which of them do actually constitute the membranes.** The performance of algorithm has been analyzed on a number of to-

tomograms that may be considered representatives of standard experimental conditions in electron tomography. In general, the algorithm has shown good behaviour as the different membranous structures present in the tomograms are successfully detected.

A quantitative analysis has also been done comparing the results obtained by our algorithm with manual segmentation over selected datasets. This comparison has been based on several metrics already employed in image segmentation and, precisely in electron tomography. Nonetheless, some modifications have been required and new metrics have had to be designed to deal with the particularities of membranes (they are relatively thin structures that are typically segmented as a set of thin contours). The outcome of this analysis suggests that our algorithm exhibits a good level of specificity and sensitivity in detecting membranes, even better than other generic segmentation methods proposed in the field ([Garduno et al., 2008](#)). These results are remarkable, as automated segmentation methods tend to 'underestimate' the object of interest compared to the manual approach ([Garduno et al., 2008](#)), which may be especially true in manual delineation of fine structures as membranes.

The algorithm has turned out to be robust as far as parameter tuning is concerned. For hysteresis thresholding, a quite similar configuration has been used in all the tests. For other stages of the algorithm, however, the parameters are highly case specific. As mentioned, their tuning is intuitive and their value can easily be estimated through simple preliminary observation of the tomogram under study.

There are several key stages in the algorithm. The very first step is the scale-space representation of the tomogram, which allows us to deal with the low SNR and contrast of tomograms and, further, to work precisely at the scale of the object

of interest. In principle, other more sophisticated denoising filters could have been used, namely anisotropic nonlinear diffusion. However, in our experience (results not shown here), the results are similar to those obtained by linear scale-space because this simple procedure helps to remove features at a scale lower than the membranes of interest. Notwithstanding, these more complex denoising methods may be of great help for the design of detectors of other structures much more complex than membranes. This is another subject of research we are conducting now.

Another key step of the algorithm is the computation of the local gauge R , a detector of local plane-ness. Nevertheless, it strongly depends on the density level. As a consequence, we defined the membrane strength M , a function reflecting the local differential structure, that overcomes the limitations of R to act as a local membrane detector. The later stages of the algorithm, hysteresis thresholding and global analysis, are intended to integrate information at a higher scale so that the true membranes are definitely extracted. In these stages, the central criterion is the number of voxels constituting the membranes, and is general enough to deal with the variety of membranous structures that can be found in tomograms. Future extensions of the algorithm to detect more complex structures will undoubtedly require more sophisticated local detectors as well as more elaborate global analysis stages.

Despite the reliability that the algorithm has shown, it still has several limitations. First of all, the effects of the missing wedge are present in the segmentation results, as easily perceptible as membranes being open along the beam direction. Sorting out this problem is not a trivial task, though some kind of modelling ([Moussavi et al., 2010](#)) may alleviate or compensate for it. This problem

also makes thin structures look like planes at local scale, such as actin filaments in the *D. discoideum* tomogram. The global analysis stages successfully deal with those false positives produced by the local detector. [The effects of the missing wedge might be attenuated by setting \$\sigma\$ and \$t_{N2}\$ to different values according to the direction.](#) Secondly, another weakness of the algorithm is the difficulty to segment, as separate objects, different membranous structures that are apposed to each other, or interacting with some other dense material, as mentioned with the HIV and mitochondrion datasets. For these cases, more complex criteria could be necessary during the global analysis stages.

The algorithm has been devised to deal with one single scale at a time. Several rounds of the algorithm allow segmentation of structures that require different scales, as illustrated with the Vaccinia dataset. Our plans for the short term include the development of a scale integration strategy that could be capable of sweeping across multiple scales and automatically selecting the proper ones for the different target structures. Such an approach would increase the robustness of the algorithm.

The algorithm has been implemented in MATLAB and the processing time ranges from minutes to a few hours, depending on the size of the tomogram. We are now developing a version in C that also makes use of high performance techniques to exploit modern multicore desktops ([Fernandez, 2008](#)). Our hope is that the resulting program is fast enough to be used with interactive tools for tomogram interpretation.

Segmentation is currently one of the major bottlenecks in the image processing workflow of electron tomography. This method for membrane delineation represents a step further towards (semi-)automated interpretation in this field. Tak-

ing into account that membranes constitute the natural limits of cells and the organelles and compartments within, their automated and objective detection will be invaluable for the analysis of the crowded and noisy environments typically imaged by electron tomography. The combination of our algorithm with other, either generic or case-specific, segmentation methods and tools already available (Volkman, 2010) will contribute to facilitating interpretation of tomograms.

Acknowledgements

The authors wish to thank Dr. O Medalia and Dr. W Baumeister for the *D. discoideum* dataset, Dr. GA Perkins for the mitochondrion dataset, and Dr. EPW Ward, Dr. TJV Yates and Dr. PA Midgley for the mesoporous silica dataset. This work has been partially supported by the Spanish Ministry of Science (MCI-TIN2008-01117), the Spanish National Research Council (CSIC-PIE200920I075) and J. Andaluca (P10-TIC-6002). AMS is a fellow of the Spanish FPI programme.

Appendix A: Response of the membrane local detector to steps

The local gauge R for membranes introduced in Section 3.2 also generates a peak for local structures that look like steps in the tomogram (see Fig. A.1). In order to make the membrane detector robust, it is thus necessary to find out and somehow remove these false positives.

In Section 3.3, the membrane strength M was introduced to give a measure of the local membrane-ness. It is a ratio between R^2 and the edge saliency S . When the values of R^2 and S for steps are analyzed, two different regions can be found (see regions A and B in Fig. A.1). In region A, steps exhibit an extremely high value of S compared to R^2 , thereby significantly attenuating the membrane strength M . However, in region B, R^2 and S may have values with similar magnitude, which may produce an unwanted peak in M . The condition shown by membranes that the slopes of R and S have opposite signs turns out to be useful to get rid of such unwanted peaks.

Appendix B: Improved hysteresis thresholding algorithm

Algorithm 1 – Improved hysteresis thresholding algorithm

N: neighbours with 6-connectivity, t_s : step

$B \leftarrow \text{get_seeds}(M, t_u, t_{N2}, t_{N3})$

$H_1 \leftarrow \text{thresholding}(M, t_o)$

$t \leftarrow t_u - t_s$

while $t \geq t_o$ **do**

$H_2 \leftarrow \text{dilation}(B, N)$

$B \leftarrow H_1 \cap H_2$

$t \leftarrow t - t_s$

end while

M denotes the input map. t_u and t_o are the undersegmenting and oversegmenting density thresholds, respectively, and t_s is the step used to progressively go from t_u to t_o during the iterative algorithm. *thresholding* and *dilation* represent those very well-known morphological operations. The neighbourhood used for dilation is the 6-connectivity (i.e. the immediate neighbours in X, Y and Z). *get_seeds* denotes the procedure described in the main text by which the input map is first undersegmented by density-thresholding with t_u and then isolated points or marginal segments are discarded by the area- and volume- thresholding procedures. The former only preserves segments in 2D planes with a number of connected voxels higher than t_{N2} . The latter considers the volume as a whole and discards 3D components with less than t_{N3} connected voxels (Fig. 4).

References

- Barcena, M., Koster, A. J., 2009. Electron tomography in life science. *Semin. Cell Dev. Biol.* 20, 920–30.
- Bartesaghi, A., Sapiro, G., Subramaniam, S., 2005. An energy-based 3D segmentation approach for the quantitative interpretation of electron tomograms. *IEEE Trans. Image Process.* 14, 1314–1323.
- Ben-Harush, K., Maimon, T., Patla, I., Villa, E., Medalia, O., 2010. Visualizing cellular processes at the molecular level by cryo-electron tomography. *J. Cell Sci.* 123, 7–12.
- Briggs, J. A., Grunewald, K., Glass, B., Forster, F., Krausslich, H. G. et al., 2006. The mechanism of HIV-1 core assembly: insights from three-dimensional reconstructions of authentic virions. *Structure* 14, 15–20.
- Cyrklaff, M., Risco, C., Fernandez, J. J., Jimenez, M. V., Esteban, M., et al., 2005. Cryo-electron tomography of vaccinia virus. *Proc. Natl. Acad. Sci. USA* 102, 2772–2777.
- Fernandez, J. J., 2008. High performance computing in structural determination by electron cryomicroscopy. *J. Struct. Biol.* 164, 1–6.
- Fernandez, J. J., 2009. TOMOBFLOW: feature-preserving noise filtering for electron tomography. *BMC Bioinformatics* 10:178.
- Fernandez, J. J., Li, S., 2003. An improved algorithm for anisotropic diffusion for denoising tomograms. *J. Struct. Biol.* 144, 152–161.

- Fernandez, J. J., Li, S., 2005. Anisotropic nonlinear filtering of cellular structures in cryoelectron tomography. *Comput. Sci. Eng.* 7 (5), 54–61.
- Fernandez, J. J., Sorzano, C. O. S., Marabini, R., Carazo, J. M., 2006. Image processing and 3D reconstruction in electron microscopy. *IEEE Signal Processing Magazine* 23(3), 84–94.
- Fernandez-Busnadiego, R., Zuber, B., Maurer, U. E., Cyrklaff, M., Baumeister, W. et al., 2010. Quantitative analysis of the native presynaptic cytomatrix by cryoelectron tomography. *J. Cell Biol.* 188, 145–156.
- Florack, L. J., Romeny, B. H., Koenderink, J. J., Viergever, M. A., 1992. Scale and the differential structure of images. *Image and Vision Computing* 10, 376–388.
- Frangakis, A. S., Hegerl, R., 2001. Noise reduction in electron tomographic reconstructions using nonlinear anisotropic diffusion. *J. Struct. Biol.* 135, 239–250.
- Frangakis, A. S., Hegerl, R., 2002. Segmentation of two- and three-dimensional data from electron microscopy using eigenvector analysis. *J. Struct. Biol.* 138, 105–113.
- Frangi, A. F., Niessen, W. J., Vincken, K. L., Viergever, M. A., 1998. Multiscale vessel enhancement filtering. *Lecture Notes in Computer Science* 1496, 130–137.
- Frank, J. (Ed.), 2006. *Electron tomography: methods for three-dimensional visualization of structures in the cell.* Springer.
- Garduno, E., Wong-Barnum, M., Volkmann, N., Ellisman, M. H., 2008. Segmen-

- tation of electron tomographic data sets using fuzzy set theory principles. *J. Struct. Biol.* 162, 368–379.
- He, W., Ladinsky, M. S., Huey-Tubman, K. E., Jensen, G. J., McIntosh, J. R. et al., 2008. Fc γ R-mediated antibody transport across epithelial cells revealed by electron tomography. *Nature* 455, 542–546.
- Koenderink, J. J., 1984. The structure of images. *Biol. Cybern.* 50, 363–370.
- Lebbink, M. N., Geerts, W. J., Krift, T. P., Bouwhuis, M., Hertzberger, L. O. et al., 2007. Template matching as a tool for annotation of tomograms of stained biological structures. *J. Struct. Biol.* 158, 327–335.
- Lindeberg, T., 1990. Scale-space for discrete signals. *IEEE Trans. Pattern Anal. Mach. Intell.* 12 (3), 234–254.
- Lindeberg, T., 1998. Edge detection and ridge detection with automatic scale selection. *Int. J. Computer Vision*, 117–154.
- Lucic, V., Forster, F., Baumeister, W., 2005. Structural studies by electron tomography: from cells to molecules. *Ann. Rev. Biochem.* 74, 833–865.
- Medalia, O., Weber, I., Frangakis, A. S., Nicastro, D., Gerisch, G. et al., 2002. Macromolecular architecture in eukaryotic cells visualized by cryoelectron tomography. *Science* 298, 1209–1213.
- Midgley, P. A., Ward, E. P., Hungria, A. B., Thomas, J. M., 2007. Nanotomography in the chemical, biological and materials sciences. *Chem. Soc. Rev.* 36, 1477–1494.

- Moussavi, F., Heitz, G., Amat, F., Comolli, L. R., Koller, D. et al., 2010. 3D segmentation of cell boundaries from whole cell cryogenic electron tomography volumes. *J. Struct. Biol.* 170, 134–145.
- Nguyen, H., Ji, Q., 2008. Shape-driven three-dimensional watersnake segmentation of biological membranes in electron tomography. *IEEE Trans. Med. Imaging* 27, 616–628.
- Perkins, G., Renken, C., Martone, M. E., Young, S. J., Ellisman, M. et al., 1997. Electron tomography of neuronal mitochondria: three-dimensional structure and organization of cristae and membrane contacts. *J. Struct. Biol.* 119, 260–272.
- Salvi, E., Cantele, F., Zampighi, L., Fain, N., Pigino, G. et al., 2008. JUST (Java User Segmentation Tool) for semi-automatic segmentation of tomographic maps. *J. Struct. Biol.* 161, 287–297.
- Sandberg, K., 2007. Methods for image segmentation in cellular tomography. *Methods in Cell Biology* 79, 769–798.
- Sandberg, K., Brega, M., 2007. Segmentation of thin structures in electron micrographs using orientation fields. *J. Struct. Biol.* 157, 403–415.
- Sato, Y., Nakajima, S., Shiraga, N., Atsumi, H., Yoshida, S. et al., 1998. Three-dimensional multi-scale line filter for segmentation and visualization of curvilinear structures in medical images. *Med. Image Anal.*, 143–168.
- Stinchcombe, J. C., Majorovits, E., Bossi, G., Fuller, S., Griffiths, G. M., 2006. Centrosome polarization delivers secretory granules to the immunological synapse. *Nature* 443, 462–465.

- Teague, M. R., 1980. Image analysis via the general theory of moments. *J. Opt. Soc. Am.* 70, 920–930.
- Udupa, J. K., LeBlanc, V. R., Zhuege, Y., Imielinska, C., Schimidt, H. et al., 2006. A framework for evaluating image segmentation algorithms. *Comput. Med. Imaging Graph.* 30, 75–87.
- van der Heide, P., Xu, X. P., Marsh, B. J., Hanein, D., Volkman, N., 2007. Efficient automatic noise reduction of electron tomographic reconstructions based on iterative median filtering. *J. Struct. Biol.* 158, 196–204.
- Volkman, N., 2002. A novel three-dimensional variant of the Watershed transform for segmentation of electron density maps. *J. Struct. Biol.* 138, 123–129.
- Volkman, N., 2010. Methods for segmentation and interpretation of electron tomographic reconstructions. *Methods Enzymol.* 483, 31–46.
- Witkin, A. P., 1983. Scale-space filtering. In: *Proc. 8th Intl. Conf. Artificial Intell.* pp. 1019–1022.
- Young, I. T., van Vliet, L. J., 1995. Recursive implementation of the gaussian filter. *Signal Processing* 44, 139–151.

Figure Legends

Figure 1. Membrane model used for the design of the local detector. (a) Membrane model in 3D. (b) Density variation along the direction perpendicular to the membrane with $D_0 = \sqrt{2\pi}$ and $\sigma_0 = 1$. (c) Second derivative L_{xx} of that membrane model ($\sigma_0 = 1$) after applying scale-space at scale $\sigma = 1$. (d) Gauges for the density profile of a membrane with $\sigma_0 = 1$ at a scale $\sigma = 1$ (blue): R^2 (red), S (cyan) and membrane strength M (green). The membrane profile, S and M are normalized in the range $[0, 1]$. R^2 keeps the scale relative to S .

Figure 2. General flow diagram of the algorithm for membrane detection.

Figure 3. Scale-space applied to a tomogram of *Dictyosleium discoideum* cell (Medalia et al., 2002). From left to right: an original 2D section of the tomogram, scale-space at $\sigma = 2$, $\sigma = 3$ and $\sigma = 4$, respectively. Dataset courtesy of Dr. O Medalia and Dr. W Baumeister.

Figure 4. Example of seed selection on a tomogram of Vaccinia virus, focused on the outer membrane. Top row: Components labelled according to their areas in three different 2D planes (along X, Y and Z). The components have been segmented by an undersegmenting thresholding process. The brightness of the labels is indicative of their area (see colormap on the right). The components that undoubtedly belong to the membrane have a larger area (larger than t_{N2} connected voxels) and appear as lighter colours. The other components (some of which also belong to the membrane) are shown in darker colours. Bottom row: The volume

is considered as a whole and the procedure only preserves those 3D components with a high number of connected voxels (higher than t_{N3}). In this row, the same three planes along X, Y and Z shown in the top row are presented for comparison. There are still some gaps in the membrane, though. As the conventional hysteresis thresholding progresses, the membrane is completely delineated.

Figure 5. The membrane segmentation approach applied to a cryo-tomogram of *D. discoideum*. A scale of $\sigma = 3$ was used. (a-f) show the same slice as in Fig. 3. (a) Gauge R . (b) Edge saliency S . (c) Membrane strength M . (d) Result of the undersegmentation process. (e) Candidates to be seeds for hysteresis thresholding. The colour is indicative of their size (see colormap in Fig. 4). The actual seeds are selected by means of the thresholds t_{N2} and t_{N3} over the size in 2D and 3D, respectively. (f) Result of the hysteresis thresholding (the same colormap is used for the labels). The colour of actin filaments has been brightened on purpose to make them noticeable in the background. (g,h) Two different views of the segmentation result. By using a threshold t_v on the size of the components in (f), the membranes are definitely extracted, (yellow). Using a different threshold t_v , the actin filaments can also be extracted (pink). Dataset courtesy of Dr. O Medalia and Dr. W Baumeister.

Figure 6. Segmentation of a Vaccinia virion obtained by cryoET. A scale of $\sigma = 3$ was used. (a) A slice of the original tomogram. (b) The same slice from the scale-space tomogram. (c) Result of the segmentation algorithm viewed in 3D. The algorithm managed to segment the outer membrane (yellow) and the core membrane (pink) using different values of the parameters σ and t_v . (d) Gauge R , (e)

edge saliency S and (f) membrane strength M resulting from the application of the algorithm.

Figure 7. Segmentation of a cryo-tomogram of HIV-1 virions. (a) A slice of the original tomogram. (b) The same slice from the tomogram at a scale $\sigma = 2$. (c) Result of the segmentation algorithm applied to extract the outer membrane of the virions, viewed in 3D. (d) Gauge R . (e) Membrane strength M . (f,g) Detail for the rightmost virion of the seed selection procedure for hysteresis thresholding, after the application of thresholds t_{N2} and t_{N3} , respectively (see colormap in Fig. 4).

Figure 8. Selected stages during segmentation of Golgi apparatus. (a) A slice of the original tomogram. (b) 3D view of the segmented structure. (c) Membrane strength M obtained with the segmentation algorithm at a scale $\sigma = 2.2$. (d) Result from the hysteresis thresholding process. The colour of the components is indicative of their size (see colormap in Fig. 4).

Figure 9. Segmentation of the membranous components of a mitochondrion. (a) A slice of the original tomogram. (b) 3D view of the segmentation result, with the outer membrane (yellow) and cristae (pink) highlighted thanks to their extraction using different values of the parameter t_v . (c) Membrane strength M obtained with the segmentation algorithm at a scale $\sigma = 1.7$. (d) Result from the seed selection for the subsequent hysteresis thresholding process (see colormap indicating the size of the components in Fig. 4). Dataset courtesy of Dr. GA Perkins.

Figure A.1. Gauges for the density profile of a step at a scale $\sigma = 2$ (blue): R^2 (red), S (cyan) and membrane strength M (green). The step and S are normalized in the range $[0, 1]$. R^2 keeps the scale relative to S . The scale used for the membrane strength M is the same as that for the M curve in Fig. 1 so as to facilitate comparison. Note that M is much lower than in the case of a true membrane. In region B, the condition that the slopes of R and S have opposite signs ensures that M is null in that region.

Figures

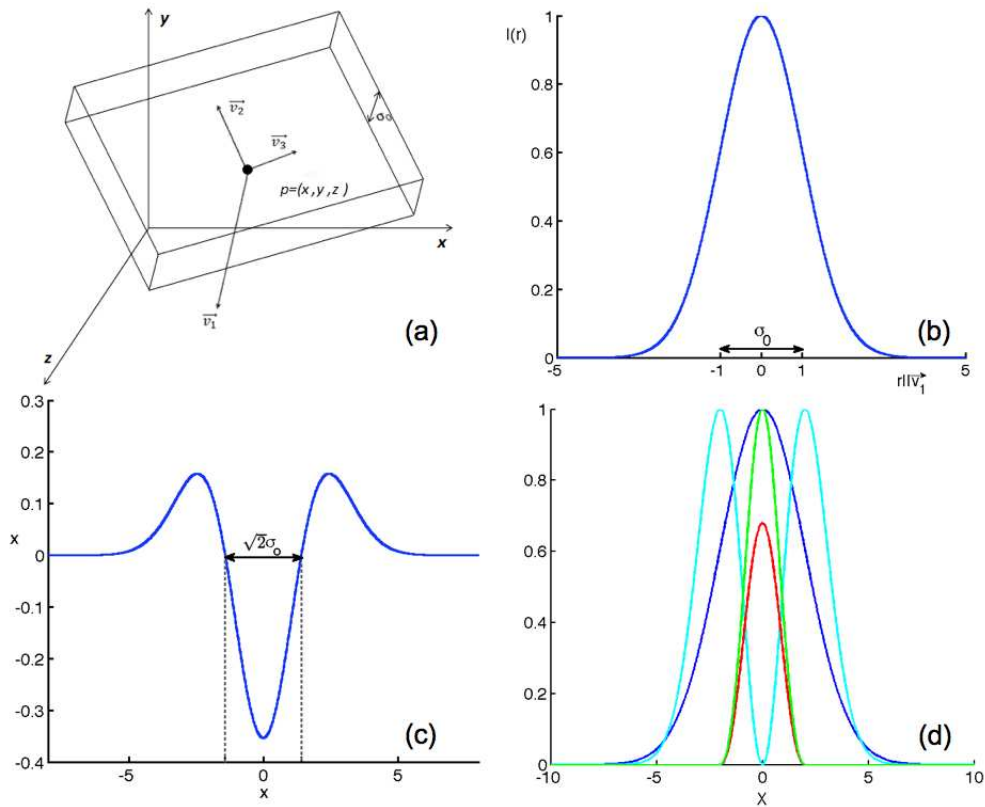


Figure 1: Membrane model used for the design of the local detector. (a) Membrane model in 3D. (b) Density variation along the direction perpendicular to the membrane with $D_0 = \sqrt{2\pi}$ and $\sigma_0 = 1$. (c) Second derivative L_{xx} of that membrane model ($\sigma_0 = 1$) after applying scale-space at scale $\sigma = 1$. (d) Gauges for the density profile of a membrane with $\sigma_0 = 1$ at a scale $\sigma = 1$ (blue): R^2 (red), S (cyan) and membrane strength M (green). The membrane profile, S and M are normalized in the range $[0, 1]$. R^2 keeps the scale relative to S .

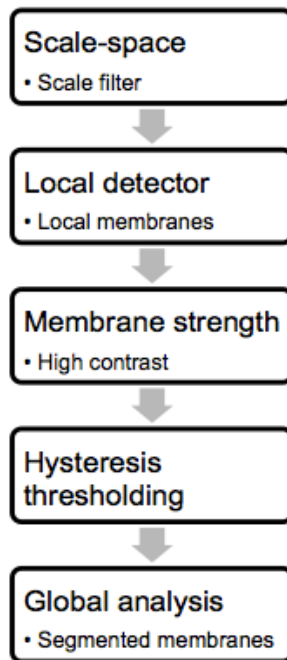


Figure 2: General flow diagram of the algorithm for membrane detection.

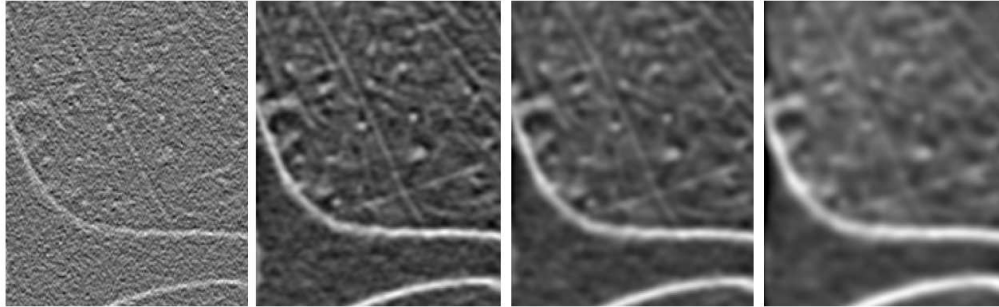


Figure 3: Scale-space applied to a tomogram of *Dictyosleium discoideum* cell ([Medalia et al., 2002](#)). From left to right: an original 2D section of the tomogram, scale-space at $\sigma = 2$, $\sigma = 3$ and $\sigma = 4$, respectively. Dataset courtesy of Dr. O Medalia and Dr. W Baumeister.

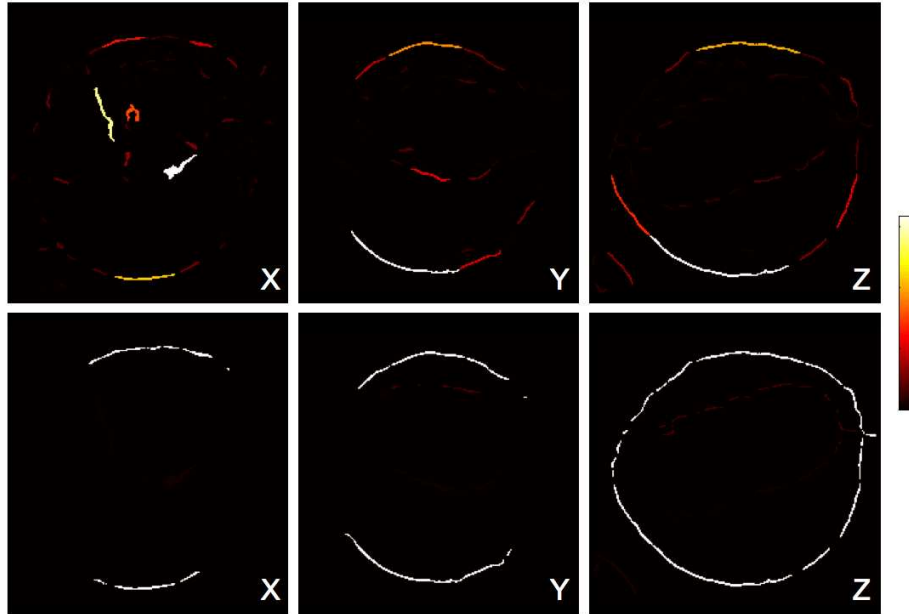


Figure 4: Example of seed selection on a tomogram of Vaccinia virus, focused on the outer membrane. Top row: Components labelled according to their areas in three different 2D planes (along X, Y and Z). The components have been segmented by an undersegmenting thresholding process. The brightness of the labels is indicative of their area (see colormap on the right). The components that undoubtedly belong to the membrane have a larger area (larger than t_{N2} connected voxels) and appear as lighter colours. The other components (some of which also belong to the membrane) are shown in darker colours. Bottom row: The volume is considered as a whole and the procedure only preserves those 3D components with a high number of connected voxels (higher than t_{N3}). In this row, the same three planes along X, Y and Z shown in the top row are presented for comparison. There are still some gaps in the membrane, though. As the conventional hysteresis thresholding progresses, the membrane is completely delineated.

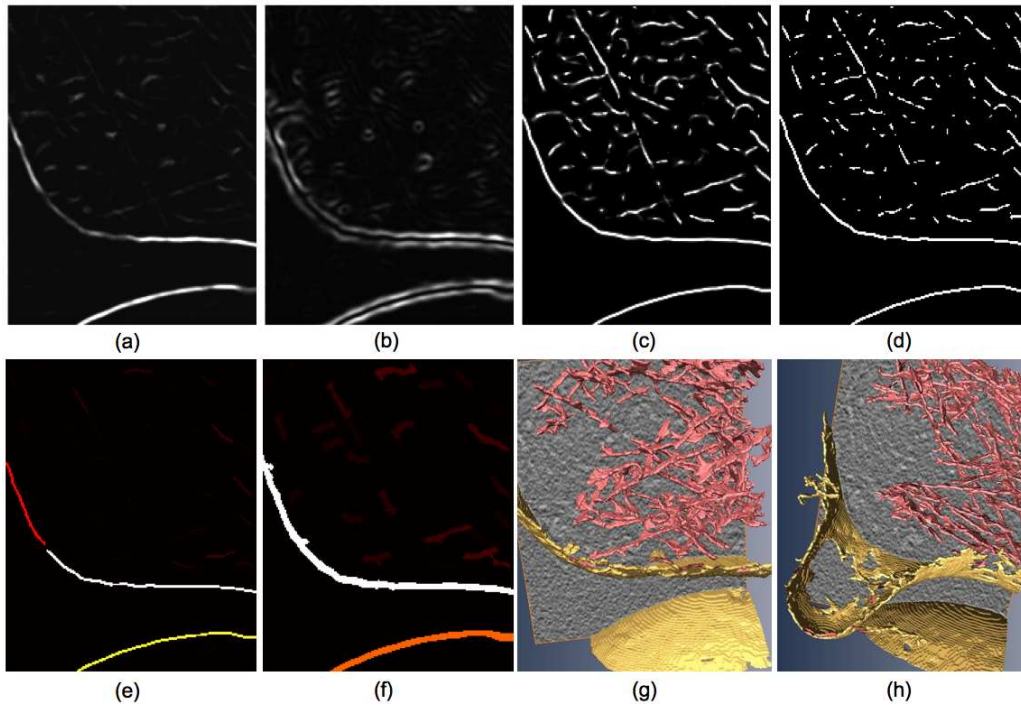


Figure 5: The membrane segmentation approach applied to a cryo-tomogram of *D. discoideum*. A scale of $\sigma = 3$ was used. (a-f) show the same slice as in Fig. 3. (a) Gauge R . (b) Edge saliency S . (c) Membrane strength M . (d) Result of the undersegmentation process. (e) Candidates to be seeds for hysteresis thresholding. The colour is indicative of their size (see colormap in Fig. 4). The actual seeds are selected by means of the thresholds t_{N2} and t_{N3} over the size in 2D and 3D, respectively. (f) Result of the hysteresis thresholding (the same colormap is used for the labels). The colour of actin filaments has been brightened on purpose to make them noticeable in the background. (g,h) Two different views of the segmentation result. By using a threshold t_v on the size of the components in (f), the membranes are definitely extracted, (yellow). Using a different threshold t_v , the actin filaments can also be extracted (pink). Dataset courtesy of Dr. O Medalia and Dr. W Baumeister.

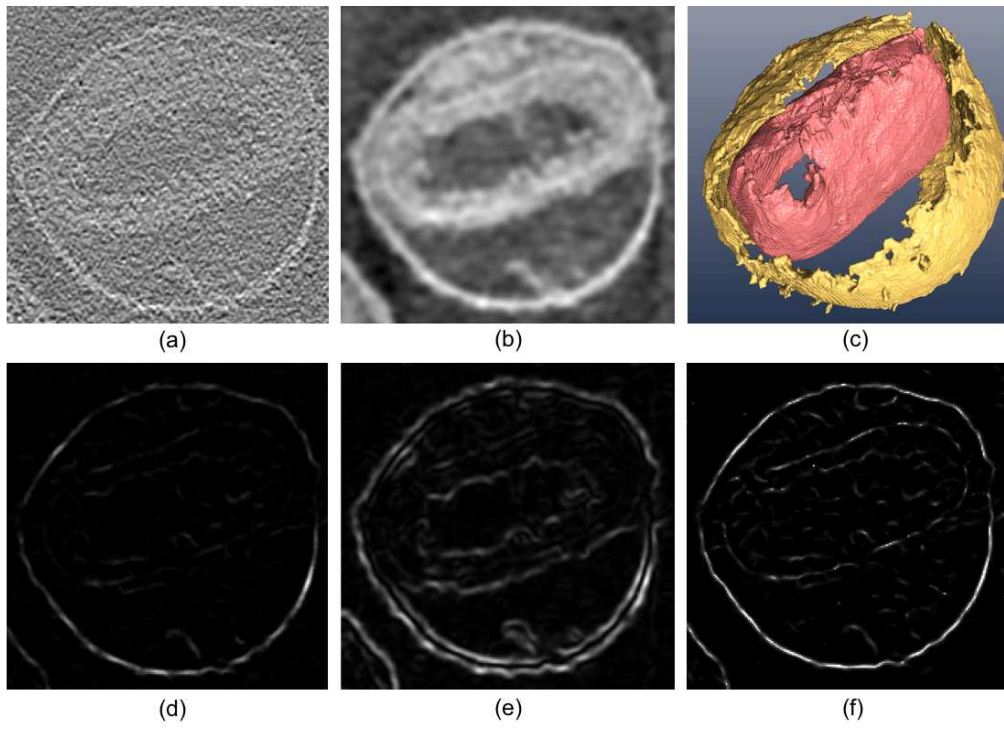


Figure 6: Segmentation of a Vaccinia virion obtained by cryoET. A scale of $\sigma = 3$ was used. (a) A slice of the original tomogram. (b) The same slice from the scale-space tomogram. (c) Result of the segmentation algorithm viewed in 3D. The algorithm managed to segment the outer membrane (yellow) and the core membrane (pink) using different values of the parameters σ and t_v . (d) Gauge R , (e) edge saliency S and (f) membrane strength M resulting from the application of the algorithm.

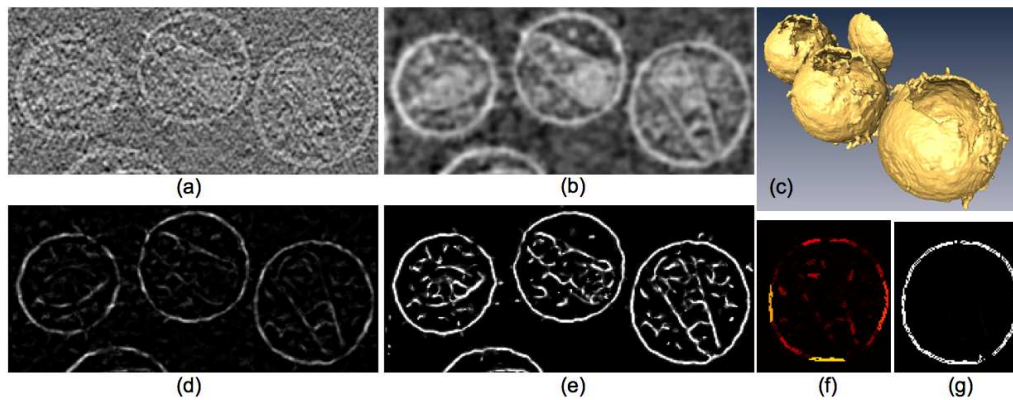


Figure 7: Segmentation of a cryo-tomogram of HIV-1 virions. (a) A slice of the original tomogram. (b) The same slice from the tomogram at a scale $\sigma = 2$. (c) Result of the segmentation algorithm applied to extract the outer membrane of the virions, viewed in 3D. (d) Gauge R . (e) Membrane strength M . (f,g) Detail for the rightmost virion of the seed selection procedure for hysteresis thresholding, after the application of thresholds t_{N2} and t_{N3} , respectively (see colormap in Fig. 4).

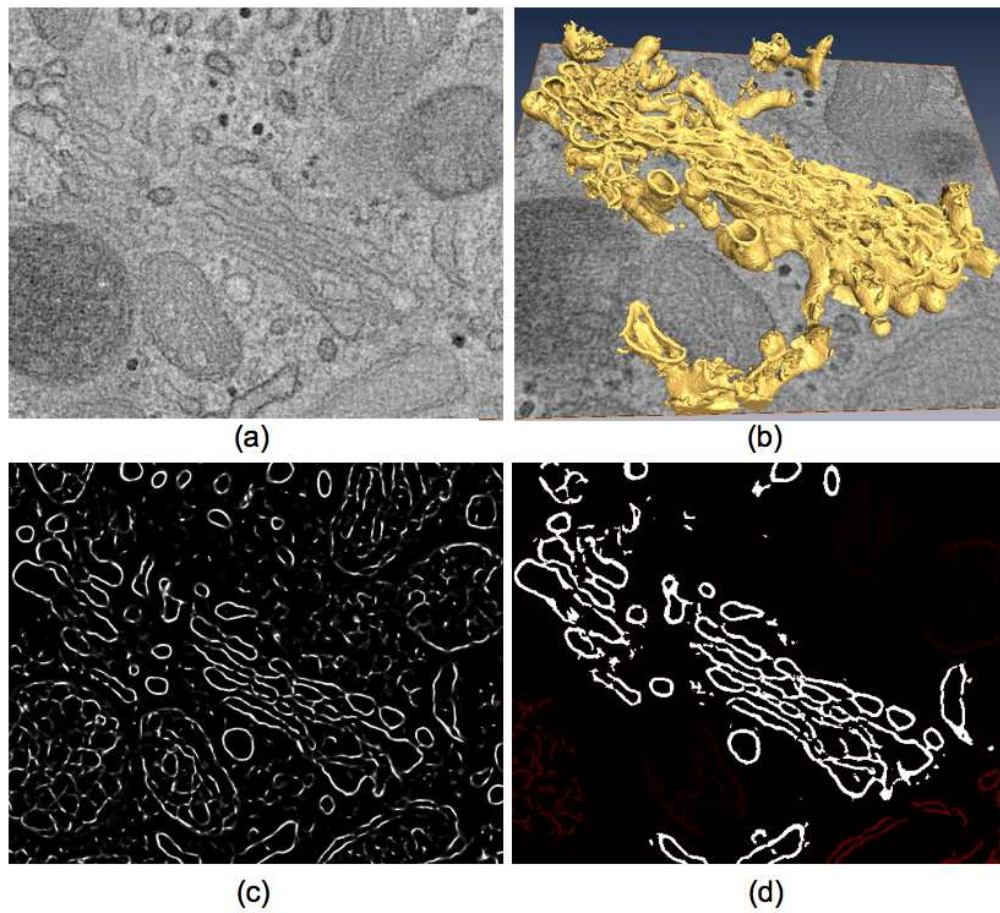


Figure 8: Selected stages during segmentation of Golgi apparatus. (a) A slice of the original tomogram. (b) 3D view of the segmented structure. (c) Membrane strength M obtained with the segmentation algorithm at a scale $\sigma = 2.2$. (d) Result from the hysteresis thresholding process. The colour of the components is indicative of their size (see colormap in Fig. 4).

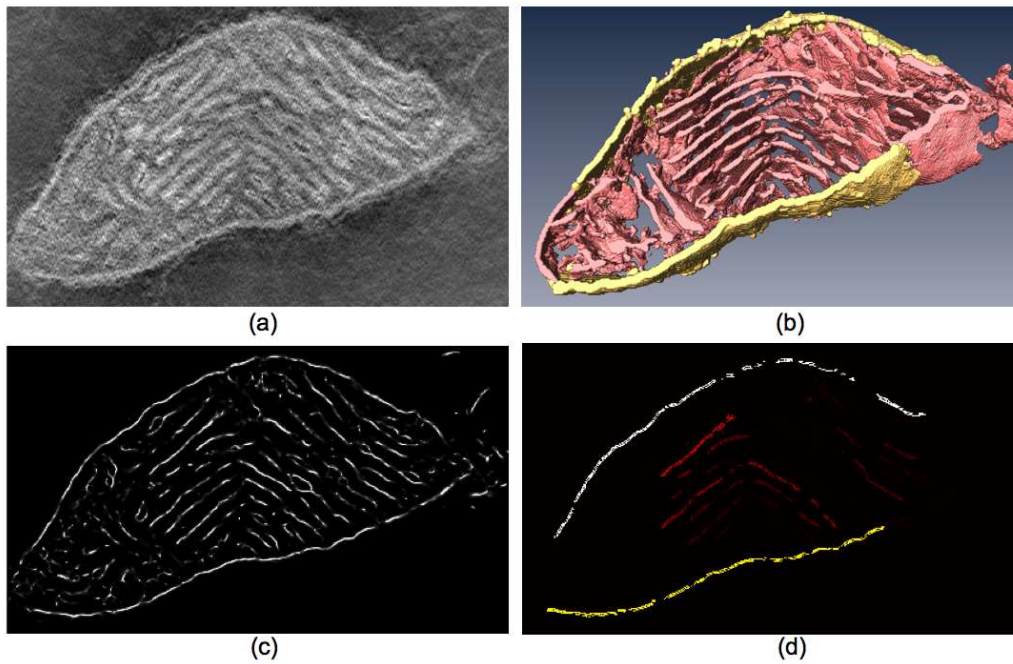


Figure 9: Segmentation of the membranous components of a mitochondrion. (a) A slice of the original tomogram. (b) 3D view of the segmentation result, with the outer membrane (yellow) and cristae (pink) highlighted thanks to their extraction using different values of the parameter t_v . (c) Membrane strength M obtained with the segmentation algorithm at a scale $\sigma = 1.7$. (d) Result from the seed selection for the subsequent hysteresis thresholding process (see colormap indicating the size of the components in Fig. 4). Dataset courtesy of Dr. GA Perkins.

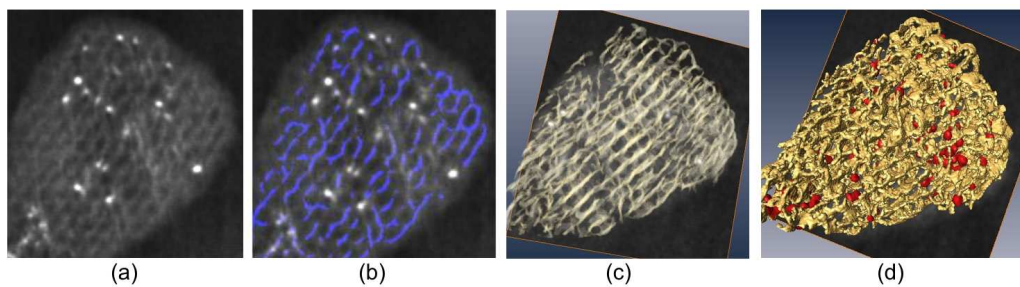


Figure 10: The segmentation algorithm helps to reveal the lattice structure of ordered silica. (a) A slice of the original tomogram. (b) Segmentation result (in blue) superimposed on the same slice. (c) Volume texture highlighting the lattice structure. (d) 3D view of the segmented structure with the silica (yellow) and the nanoparticles (red). Dataset courtesy of Dr. EPW Ward, Dr. TJV Yates and Dr. PA Midgley.

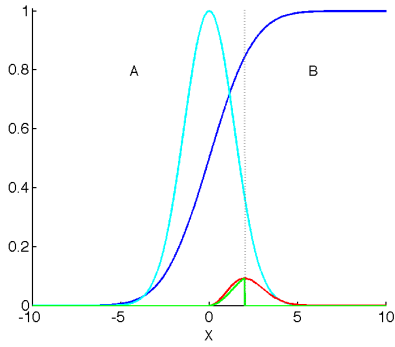


Figure A.1: Gauges for the density profile of a step at a scale $\sigma = 2$ (blue): R^2 (red), S (cyan) and membrane strength M (green). The step and S are normalized in the range $[0, 1]$. R^2 keeps the scale relative to S . The scale used for the membrane strength M is the same as that for the M curve in Fig. 1 so as to facilitate comparison. Note that M is much lower than in the case of a true membrane. In region B, the condition that the slopes of R and S have opposite signs ensures that M is null in that region.

Tables

Table 1: Quantitative analysis of the membrane segmentation algorithm vs. manual annotation

Data	Bounding box			Centroid	Axes		TPF	TNF
	Centre	Width	Height		Major	Minor		
Vaccinia	98.88	97.29	98.38	97.64	96.53	95.35	92.63	98.01
Golgi	98.53	97.92	96.41	98.51	90.27	93.02	92.20	97.90